



Cite this: *Energy Environ. Sci.*, 2019, 12, 3182

## Ultra-flexible perovskite solar cells with crumpling durability: toward a wearable power source†

Gunhee Lee,<sup>‡,ab</sup> Min-cheol Kim,<sup>‡,ac</sup> Yong Whan Choi,<sup>ad</sup> Namyoun Ahn,<sup>a</sup> Jihun Jang,<sup>a</sup> Jungjin Yoon,<sup>a</sup> Sang Moon Kim,<sup>ib</sup> Jong-Gu Lee,<sup>f</sup> Daeshik Kang,<sup>ig</sup> Hyun Suk Jung<sup>ib,\*h</sup> and Mansoo Choi<sup>ib,\*ab</sup>

Perovskite materials hold great potential as photovoltaic power sources for portable devices owing to their mechanical flexibility and high performance; however, the flexibility and efficiency require further improvement to attain practical viability. We investigated the mechanical fracture behavior of polycrystalline perovskite films by varying the substrate thickness and applying the neutral plane concept. This enabled us to fabricate a crack-free perovskite film on an ultra-thin substrate ( $\sim 2.5 \mu\text{m}$ ) and to demonstrate ultra-flexible solar cells with high efficiency (17.03%) with unprecedented flexibility sustained after 10 000 cycles of bending at a 0.5 mm radius. This represents a high efficiency of 13.6% for large-area flexible perovskite solar cells ( $1.2 \text{ cm}^2$ ), fabricated by using a hybrid transparent electrode composed of a metal mesh grid and conducting polymer. Using a protective layer to achieve the neutral plane concept, our ultra-flexible perovskite solar cells are demonstrated to be durable even after 100 crumpling cycles. Our approach paves the way to fabricate flexible perovskite solar cells for portable power sources.

Received 18th June 2019,  
Accepted 20th September 2019

DOI: 10.1039/c9ee01944h

rsc.li/ees

### Broader context

There will be increasing demand for lighter, flexible, longer-lasting, and high-performance portable power sources. Perovskite solar cells (PSCs) have been regarded as a promising candidate for portable application because of their good performance, flexibility and low-cost fabrication, however, extreme mechanical durability such as crumpling and folding has not been demonstrated yet. This work demonstrated ultra-flexible PSCs with a best power conversion efficiency (PCE) of 17.03% that can withstand 100 cycles of crumpling and 10 000 cycles of bending ( $R = 0.5 \text{ mm}$ ) for the first time. The PSCs were fabricated on ultra-thin substrates ( $\sim 2.5 \mu\text{m}$ ) and covered by a parylene protective layer in order to locate the neutral plane on the perovskite layer to cause the total strain to be a minimum. Large-area flexible PSCs ( $1.2 \text{ cm}^2$ ) were also achieved with a best PCE of 13.6% by using a hybrid transparent electrode composed of a metal mesh grid and a conducting polymer.

<sup>a</sup> Global Frontier Center for Multiscale Energy Systems, Seoul National University, Seoul, Republic of Korea. E-mail: hsjung1@skku.edu, mchoi@snu.ac.kr

<sup>b</sup> Department of Mechanical Engineering, Seoul National University, Seoul, Republic of Korea

<sup>c</sup> Department of NanoEngineering, University of California, San Diego, 9500 Gilman Drive, LaJolla, California 92093, USA

<sup>d</sup> Division of Mechanical Convergence Engineering, Silla University, Busan, Republic of Korea

<sup>e</sup> Department of Mechanical Engineering, Incheon National University, Incheon, 406-772, Republic of Korea

<sup>f</sup> School of Mechanical and Aerospace Engineering/IAMD, Seoul National University, Gwanak 599, Gwanak-ro, Gwanak-gu, Seoul 151-742, Republic of Korea

<sup>g</sup> Department of Mechanical Engineering, Ajou University, San 5, Woncheon-dong, Yeongtong-gu, Suwon 443-749, Republic of Korea

<sup>h</sup> School of Advanced Materials Science & Engineering, Sungkyunkwan University, Suwon, Gyeonggi-do, Republic of Korea

† Electronic supplementary information (ESI) available. See DOI: 10.1039/c9ee01944h

‡ These authors contributed equally to this work.

## Introduction

Flexible and lightweight photovoltaics are promising candidates to power portable and wearable electronic applications such as deformable displays, electronic textiles, and artificial skin.<sup>1–3</sup> In particular, organic–inorganic halide perovskite materials for functional photovoltaics have attracted considerable interest as suitable power sources for these applications owing to their high power conversion efficiency (PCE), low-temperature processing, and low-cost fabrication.<sup>4–7</sup> In recent years, these advantageous properties have prompted the development of flexible perovskite solar cells *via* various engineering approaches such as the introduction of additive materials,<sup>8–10</sup> advancing the device structure,<sup>11,12</sup> substitution of the brittle transparent electrode with graphene,<sup>13–15</sup> employing carbon nanotubes,<sup>16,17</sup> incorporating silver nanowires<sup>18,19</sup> and using highly conductive polymers.<sup>20,21</sup>

However, existing flexible perovskite photovoltaics continue to remain far from practical for application in portable devices owing to their lack of bending durability. Many previous research efforts only conducted cyclic bending tests for flexible perovskite solar cells at large bending radii for a few thousand cycles.<sup>22,23</sup> In most cases, after lenient bending tests, the perovskite films develop cracks, which are directly responsible for performance degradation.<sup>17,21,24</sup> Perovskite devices with such inferior deformation durability are unsuitable for practical flexible devices because severe deformation such as complete crumpling and/or folding could occur during actual operation.<sup>25,26</sup> Therefore, further studies on the flexibility and mechanical properties of perovskite photovoltaics are necessary to advance portable power sources. Previous studies on the mechanical properties of perovskite materials have mainly focused on single-crystal perovskites.<sup>27,28</sup> Accordingly, it is necessary to seek the deformation limits of polycrystalline perovskite thin films for the purpose of developing flexible applications. However, investigating the mechanical properties of polycrystalline perovskite thin films is challenging because it is difficult to perform nano-indentation testing or direct measurements of the elastic, plastic, and fractural responses of perovskite thin films. Therefore, it is essential to explore the mechanical fracture points of these thin films by carrying out indirect measurements; for example, by controlling the amount of strain applied to the surface of the perovskite film. In addition, it is of crucial importance to develop large-area flexible devices with high photovoltaic performance to extend their practical applicability.

Herein, we used morphological observations by scanning electron microscopy (SEM) measurements, and finite element method (FEM) simulation to identify the relationship between crack formation and the strain applied to perovskite films. This approach enabled us to determine the mechanical fracture points of the polycrystalline perovskite films. On the basis of our improved understanding of the mechanical properties of perovskite thin films, we were able to achieve remarkable bending durability results. These results allowed us to fabricate crack-free perovskite films on ultra-thin poly(ethylene terephthalate) (PET) substrates ( $\sim 2.5 \mu\text{m}$ ) with the aid of poly(dimethylsiloxane) (PDMS) supports, which cannot be realized by using PET substrates of typical thickness (30–100  $\mu\text{m}$ ). While ultra-thin plastic substrates have been introduced for lightweight perovskite solar cells before, previous studies have only focused on high power per weight.<sup>20,29</sup> In this report, on account of our further understanding of the mechanical behavior, we were able to demonstrate ultra-flexible perovskite solar cells (with a PCE of 17.03%) that maintain their initial performance after 10 000 bending cycles at a bending radius of 0.5 mm; this result surpasses the best bending durability reported thus far. In addition, we successfully demonstrated large-area flexible perovskite solar cells (13.6%) with an active area of  $1.2 \text{ cm}^2$ . These cells do not include a conducting oxide as the transparent electrode, which was replaced by hybrid transparent electrodes consisting of a conducting polymer and a metal mesh grid. Furthermore, we enhanced their potential use in wearable applications by adding a parylene protective layer to modulate the neutral plane axis such that it lies on the perovskite layer

(*i.e.*, the strain applied to the layer becomes almost zero). The introduction of the protective layer on top of the complete large-area solar cell enabled us to obtain perovskite solar cells capable of enduring crumpling deformation tests of more than 100 cycles for the first time. This result means that crumpling durable perovskite solar cells with protective layer can endure the wrinkles of clothes when they are utilized in wearable applications. The successful construction of this ultra-flexible perovskite solar cell with a large active area and high efficiency, and which is able to endure harsh deformation (small radius bending, crumpling, and folding), is a breakthrough that is expected to lead to the further development of our device as a commercially viable portable power source.

## Results and discussion

### Concept of ultra-flexible perovskite solar cells

The successful fabrication of ultra-flexible perovskite solar cells requires the deposition of a high-quality perovskite film coating on an ultra-thin polymer substrate ( $\sim 2.5 \mu\text{m}$ ). However, the spin-coating process, which is usually used to fabricate these solar cells, easily fails when attempting to apply the coating to an ultra-thin PET substrate. Thus, it is necessary to stabilize the process of fabricating flexible perovskite solar cells to avoid technical problems due to wrinkling or folding of the ultra-thin flexible substrate (Fig. 1a). This could be achieved by taking advantage of the conformal contact of PDMS. We used PDMS layers between  $2.5 \mu\text{m}$  thick PET and rigid glass substrates as a supporting fixture and obtained a firm substrate that neither wrinkles nor folds during the full fabrication procedure (Fig. 1a). As the complete device including the PET film could be easily detached from the PDMS/rigid substrate at the end of fabrication, the use of PDMS enabled us to fabricate flexible devices without handling problems. We prepared perovskite solar cells with p-i-n structure (poly(3,4-ethylenedioxythiophene)-polystyrene sulfonate (PEDOT:PSS)/ $\text{CH}_3\text{NH}_3\text{PbI}_3(\text{MAPbI}_3)/\text{C}_{60}/\text{bathocuproine}(\text{BCP})/\text{Cu}$ ) without the brittle transparent conducting oxide (TCO), as shown in Fig. S1 (ESI<sup>†</sup>). The purpose of removing the brittle TCO is to prohibit crack propagation on this layer in advance.<sup>30</sup> Finally, we achieved highly efficient flexible perovskite solar cells with homogeneous PEDOT:PSS and  $\text{MAPbI}_3$  layers regardless of the thickness of the PET substrates (three different thicknesses were investigated: 100, 30, and  $2.5 \mu\text{m}$ ). The average PCEs of the three devices have comparable values, as summarized in Fig. 1b in the form of box charts. These results confirmed the reliability of our method to fabricate flexible devices and made it possible to proceed with our analysis of the mechanical properties. We therefore analyzed the fractural behavior of the perovskite thin films with uniform quality by changing the strain that was applied to the perovskite film by adjusting the substrate thickness and bending radius (Fig. 1c). In an attempt to further improve the mechanical stability of the perovskite thin films, we manipulated the neutral plane (NP) axis formation region by introducing a protective layer in the form of a parylene thin film (Fig. 1d). As can be seen in Fig. 1d, the NP axis,

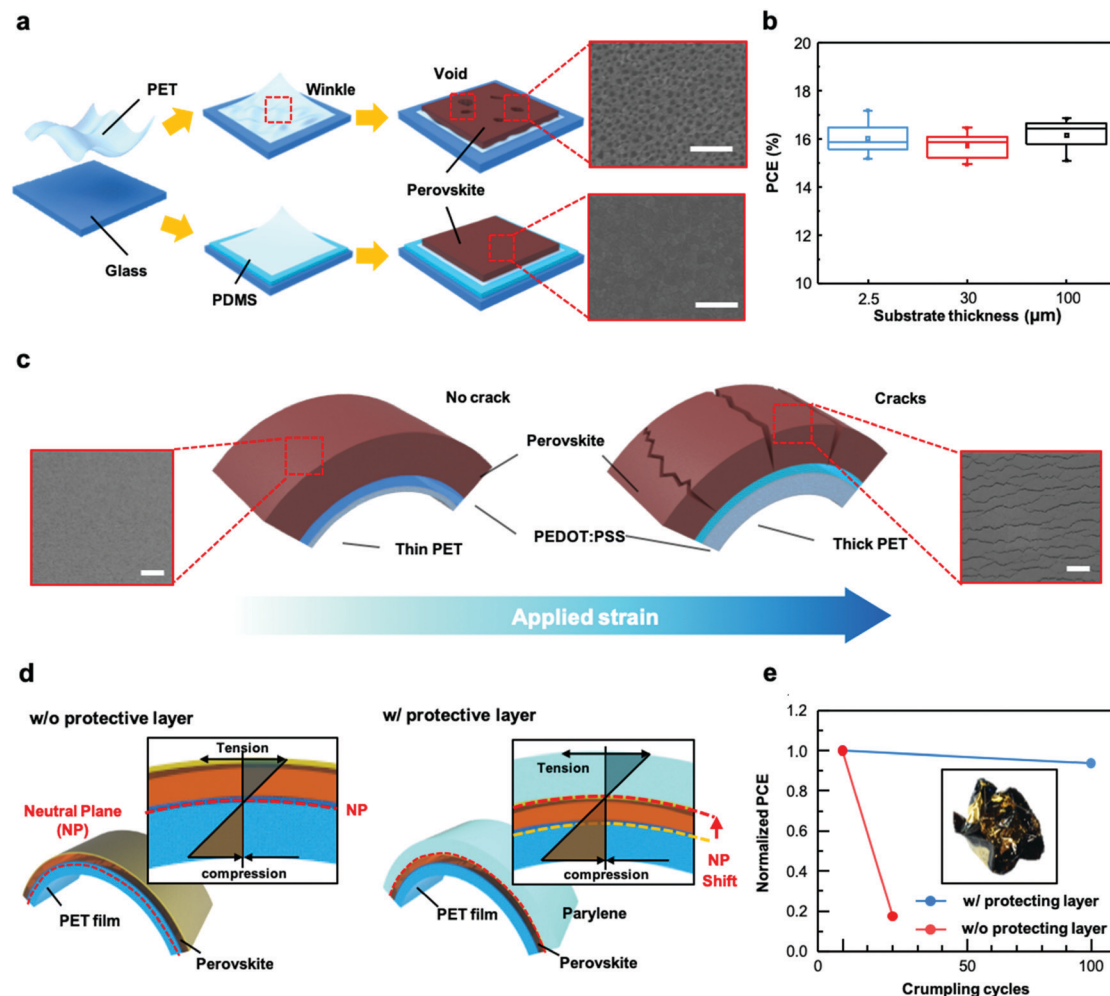


**Fig. 1** Graphical illustration of the different perovskite films. (a) Dependence of the quality on the existence of poly(dimethylsiloxane) (PDMS). (b) Box plots of the power conversion efficiency (PCE) of three devices with different substrate thicknesses (2.5, 30, and 100  $\mu\text{m}$ ). (c) Schematic illustrations of the substrate thickness in the perovskite film upon sustainable bending. (d) Illustrations of perovskite solar cells without and with a protective layer consisting of a parylene film. (e) Normalized PCE of the devices as a function of the number of crumpling cycles without and with the protective layer.

which is firstly formed at PEDOT:PSS, shifts up to the perovskite films with the application of the protective layer. This layer not only modulates the NP axis, which is the plane in which the applied strain equals zero, located at the perovskite layer, but also protects the layer against scratching or contamination by the exterior environment. Introduction of the protective layer enabled us to obtain ultra-flexible solar cells with excellent durability against crumpling. Specifically, these cells maintain their initial performance of up to 88% after 100 cycles of crumpling, whereas those without the protective layer rapidly degrade after 20 cycles of crumpling.

#### Degradation and mechanical fracture behavior as a function of substrate thickness

The achievement of a crack-free perovskite thin film and ultra-flexible perovskite solar cells with good crumpling durability inevitably requires an evaluation of the performance of the perovskite solar cells by varying the substrate thickness to confirm the effect of applied strain. First, we compared the

efficiency of devices, fabricated on substrates with three different thicknesses, before and after bending, by subjecting the perovskite solar cells to a bending cyclic test. Fig. S2 (ESI<sup>†</sup>) shows the  $J-V$  curves of the three devices before and after the bending test of 1000 cycles at a bending radius ( $R$ ) of 0.5 mm. Surprisingly, the flexible perovskite photovoltaics, which exhibit equivalent initial efficiencies, have entirely different final efficiencies after 1000 bending cycles, depending on the substrate thickness. Hereafter, we denote devices with a PET substrate with a thickness of  $d$   $\mu\text{m}$  as a  $d$ -PET device for the sake of simplicity. In the case of the 2.5-PET device, the  $J-V$  curves hardly changed after 1000 cycles of bending, whereas both the 30-PET and 100-PET devices experienced severe performance degradation under the same conditions. We subsequently examined the performance degradation and generation of cracks during repeated bending by performing detailed cyclic bending tests with two bending radii ( $R = 1$  and 0.5 mm) and different substrate thicknesses and measured the evolution of the photovoltaic performance and morphologies (Fig. 2a-i). In the case of the 2.5-PET device, neither

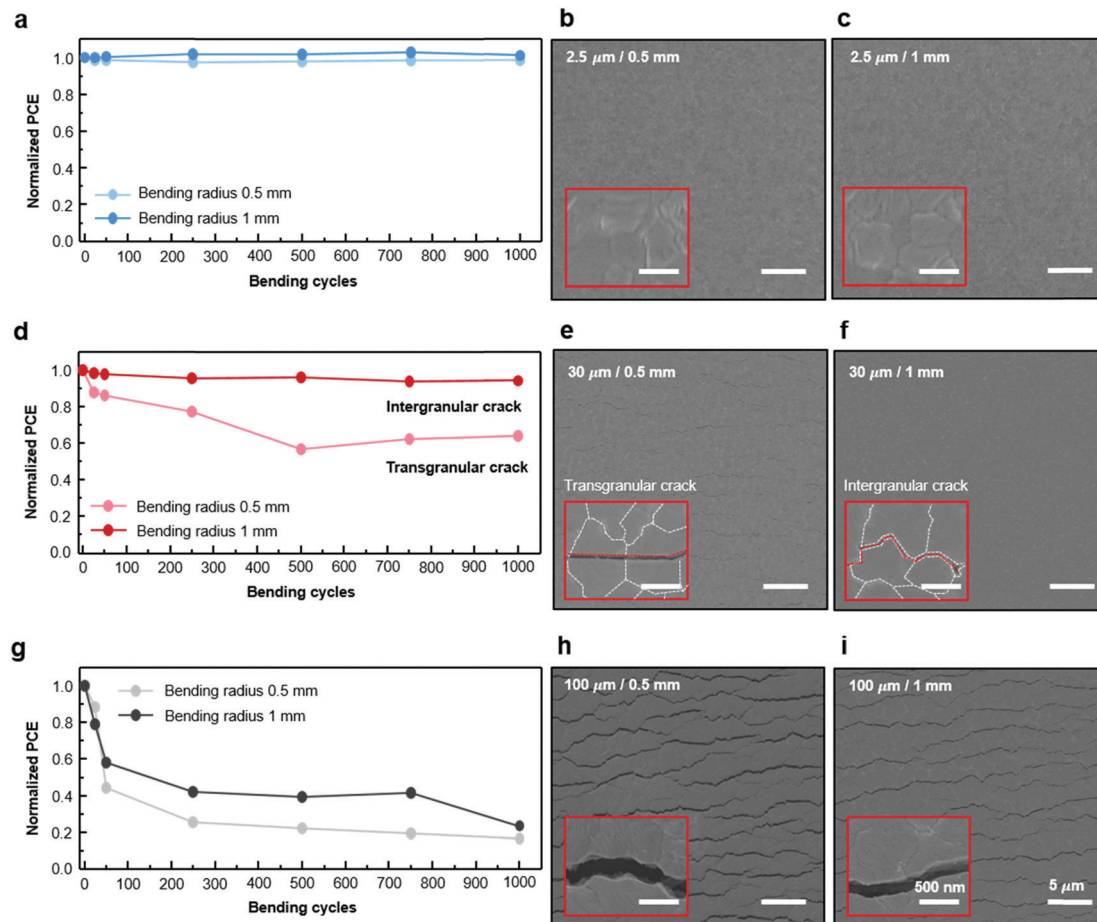


Fig. 2 Normalized power conversion efficiencies (PCEs) as a function of bending cycles and corresponding scanning electron microscope (SEM) images. Substrates have thicknesses of (a) 2.5 μm, (d) 30 μm, and (g) 100 μm at bending radii of 0.5 and 1 mm. SEM images of the perovskite film after bending cyclic tests for substrate thicknesses of (b and c) 2.5 μm, (e and f) 30 μm, and (h and i) 100 μm at bending radii of 0.5 and 1 mm.

the performance nor the surface morphology changed after 1000 bending cycles at both bending radii, as shown in Fig. 2b and c. On the other hand, the 100-PET device with the thickest substrate showed significant performance degradation and a number of deep cracks with gaps the size of a few hundred nanometers for both bending radii (Fig. 2h and i). The evolution of the PCE is mainly attributed to the lower MAPbI<sub>3</sub> film quality due to the formation of deep and wide cracks. Notably, for the 30-PET device, ~95% of its initial value was preserved at a bending radius of 1 mm, whereas the PCE of the same device degrades to ~65% of its original value at a bending radius of 0.5 mm, as can be seen in Fig. 2d. After 1000 cycles, the surface morphologies also displayed distinct characteristics according to the different bending radii. In the case of  $R = 1$  mm, cracks formed along the grain boundaries, whereas deep and long cracks appeared through individual MAPbI<sub>3</sub> grains in the case of  $R = 0.5$  mm (Fig. 2e and f). The absence of cracks on the PEDOT:PSS surface deposited on the 30-PET substrate after 1000 cycles of bending at 0.5 and 1 mm bending radii (Fig. S3, ESI<sup>†</sup>) suggests that the cracks originated from the perovskite surface. That is, the performance reduction is highly associated with the overall crack densities of the MAPbI<sub>3</sub> films. This result provides a considerable advance toward our understanding of the mechanical

properties of polycrystalline perovskite thin films. Generally, as mentioned above, the mechanical properties of materials are characterized by performing nano-indentation measurements or by density functional theory calculations. Research using both of these approaches to examine the mechanical properties of metal halide perovskite materials has been reported. However, both approaches only precisely correspond to single-crystalline perovskite materials on account of the difficulty associated with the measurement of thin films and the limitation of having to make assumptions in simulation. Thus, it is difficult to determine the deformation limit or degradation point of a perovskite polycrystalline thin film that is actually used in a device. The experimental results we have presented here show, for the first time, the deformation limit of polycrystalline MAPbI<sub>3</sub> thin films (Fig. 3a). The generation of cracks and their densities depend on both the substrate thickness and bending radius, which is indicative of the strain-dependent yield characteristics of the films. More particularly, as can be seen in Fig. 3a, a crack-free region exists at an applied strain of ~1.4%, which can be identified in the case of 2.5-PET (no cracks). A crack propagation region, which indicates that cracks propagated along the grain boundaries, exists between ~1.4% and ~2.8% applied strain

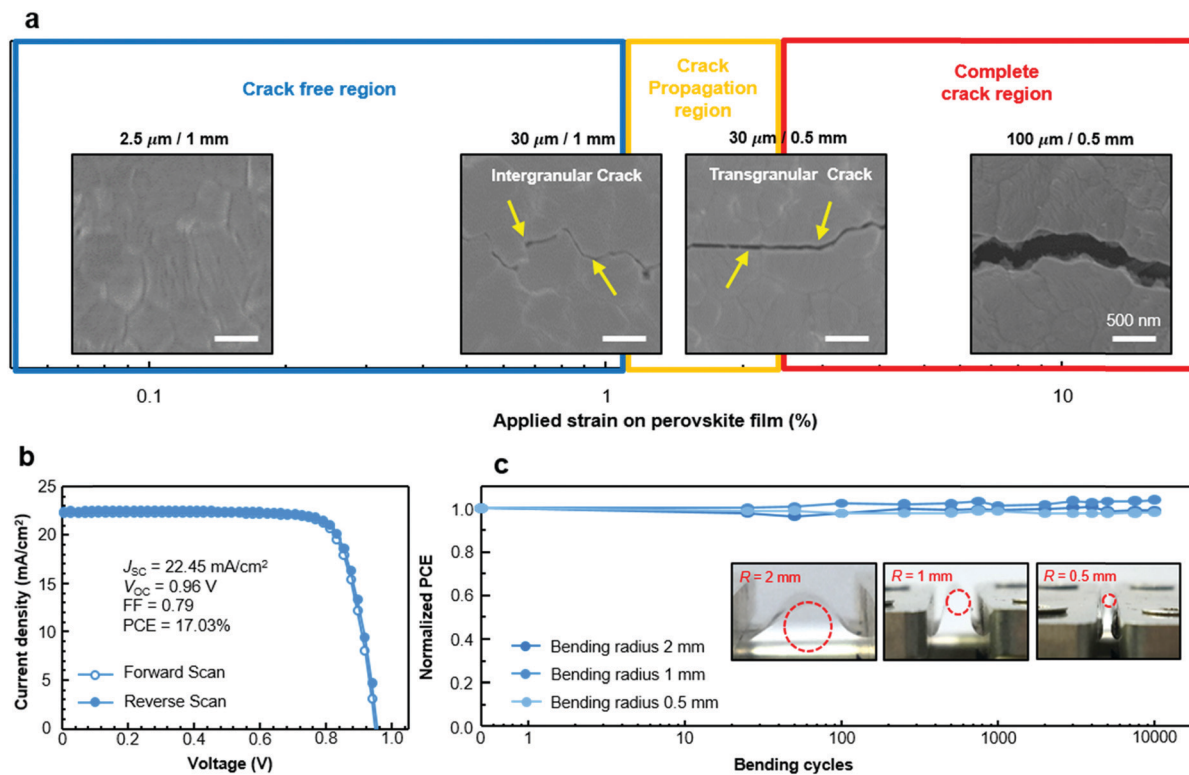


Fig. 3 (a) Relationship between crack formation and strain applied to the perovskite film based on finite element method (FEM) results and scanning electron microscope (SEM) images. (b) Reverse and forward bias  $J-V$  curves of the perovskite solar cell with the 2.5 μm thick substrate. (c) Normalized power conversion efficiencies (PCEs) as a function of bending cycle depending on the bending radius ( $R = 2, 1, \text{ and } 0.5 \text{ mm}$ ) for the 2.5 μm thick substrate. The photographic images in the inset show the device bent at various bending radii.

(see 1 mm bending with 30-PET; intergranular cracks). Finally, a complete crack region is found to exist, which means that the cracks generated on the grain start after the applied strain reaches 2.8% (see 0.5 mm bending in the 30-PET and 100-PET cases; transgranular cracks). In support of these results, we additionally performed FEM simulations, as can be seen in Fig. S4 (ESI<sup>†</sup>), which revealed that the thicker the substrate and the smaller the bending radius, the more the strain that is applied to the device.

#### Achieving ultra-flexible perovskite solar cells using an ultra-thin substrate

Based on our experimental results and analysis, we adopted an ultra-thin substrate for excellent device flexibility. Additional experiments were performed to determine whether the perovskite film could tolerate even harsher bending conditions. The fact that the 2.5-PET device presents the highest bending durability among all the cases (Fig. 2) with the absence of cracks generated on the perovskite films indicates that we succeeded in optimizing the device performance. Furthermore, we confirmed the endurance of the flexible devices under intensive deformation conditions (10 000 bending and crumpling cycles), which is an essential requirement for portable device applications. The use of the 2.5 μm thick PET substrate enabled us to achieve a 17.03% PCE with a short-circuit current density ( $J_{sc}$ ) of 22.45 mA cm<sup>-2</sup>, an open-circuit voltage ( $V_{oc}$ ) of 0.96 V, a fill factor (FF) of 0.79,

and negligible hysteresis for the devices that exhibited the best performance, as shown in Fig. 3b. We used the PDMS-assisted fabrication method, as illustrated in Fig. 1, to fabricate 45 devices, thereby verifying the reproducibility of the 2.5-PET-based perovskite solar cells, as depicted in Fig. S5 (ESI<sup>†</sup>). The average values of the photovoltaic parameters for the 2.5-PET devices are summarized in Table S1 (ESI<sup>†</sup>), providing additional evidence of their reproducibility. We also measured the stabilized current density and external quantum efficiency (EQE) as shown in Fig. S6 (ESI<sup>†</sup>), which are in good agreement with the  $J-V$  curve measurements.

We examined the durability of the flexible perovskite devices under harsh conditions by carrying out cyclic bending tests at various bending radii ( $R = 2, 1 \text{ and } 0.5 \text{ mm}$ ) for 10 000 cycles, as shown in Fig. 3c and Fig. S7 (ESI<sup>†</sup>). Noteworthy is that the 2.5-PET device does not undergo performance degradation at all after 10 000 cycles of bending at either bending radius (Fig. 3c). The inset images show detailed results of the bending tests according to the various bending radii. This is the first report in which the durability of flexible perovskite solar cells is demonstrated even after 10 000 bending cycles.

#### Highly efficient large-area flexible device using modulated electrodes

Despite the promising result (*i.e.*, the 2.5-PET device was able to endure 10 000 cycles of bending), actual application of these

devices remains limited because of their small active area ( $\sim 0.1 \text{ cm}^2$  for each device). It therefore remains a challenge to fabricate large-area flexible perovskite solar cells with both high mechanical durability and performance considering the lower electrical conductivity of bending durable electrodes compared with brittle conducting oxide. In an attempt to overcome the trade-off between bending durability and conductivity, we introduced a gold metal mesh grid beneath the conducting polymer. This approach enabled us to successfully fabricate perovskite solar cells (Fig. 4a) containing hybrid transparent electrodes that have high lateral conductivity (Table S2, ESI<sup>†</sup>). The metal mesh grid leads to a slight loss of transmittance by reflecting the incident light; however, this does not have any noticeable effect on the device performance (Fig. 4b). As a result, the performance of the device with the gold mesh dramatically increased compared with the device without it (Fig. 4c). Finally, we improved the efficiency to as much as 13.62% for an active area of size  $1 \text{ cm}^2$  (Fig. 4c). The reproducibility of the large-area flexible perovskite solar cells was verified by recording histograms of 20 devices, as shown in Fig. S8 (ESI<sup>†</sup>). All photovoltaic parameters are summarized in Table S1 (ESI<sup>†</sup>). Potential issues could involve

the non-uniform coating of the charge transport layer on top of the metal grid. This could be resolved by optimizing the metal grid geometry or by using a deposition method with better step coverage.<sup>31,32</sup>

Furthermore, we performed cyclic bending tests for both the PEDOT:PSS/metal mesh grid/PET and the MAPbI<sub>3</sub>/PEDOT:PSS/metal mesh grid/PET samples in order to verify that the introduction of the metal mesh grid affects the flexibility of the device. Observations of the morphology of the hybrid electrodes consisting of a metal mesh grid and PEDOT:PSS enabled us to confirm that the hybrid electrode is not destroyed at all after bending, as shown in Fig. 4d. In addition, the perovskite surface contains no cracks after 1000 cycles of bending (Fig. 4d). Based on these results, we conclude that the large-area device has superior bending durability and the hybrid electrode based on the metal mesh does not detrimentally affect the photovoltaic performance to any significant extent after bending. As a consequence of the absence of morphological change, no performance degradation was observed after 1000 cycles of bending at  $R = 1$  and  $0.5 \text{ mm}$  (Fig. 4e).

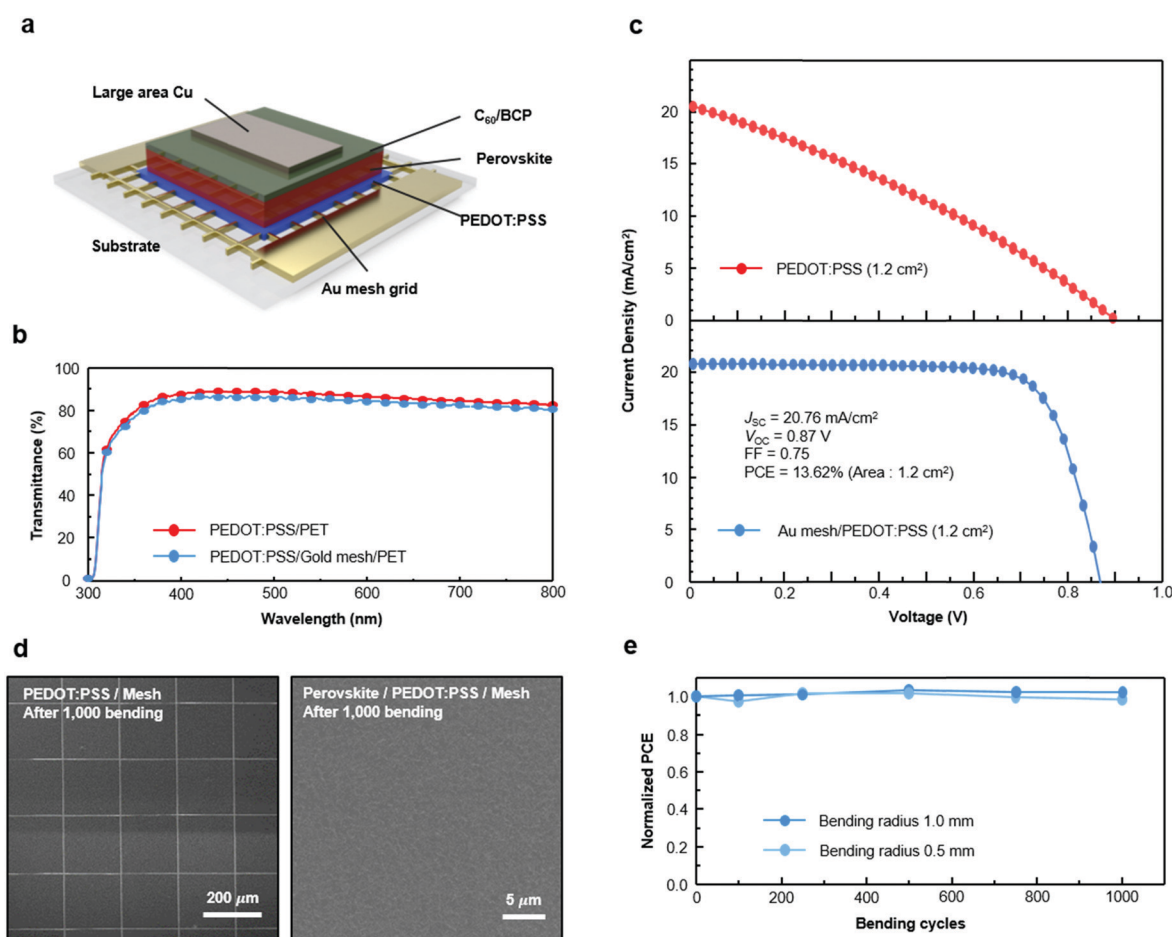


**Fig. 4** (a) Schematic illustration of the structure of the cell incorporating a gold mesh grid. (b) Transmittance of the PEDOT:PSS/PET and PEDOT:PSS/gold mesh/PET substrates. (c)  $J$ - $V$  curves of the large-area device ( $1.2 \text{ cm}^2$ ) with and without the gold mesh grid. (d) Scanning electron microscope (SEM) images of the hybrid electrode (gold mesh and PEDOT:PSS) and perovskite film after bending tests. (e) Normalized power conversion efficiencies (PCEs) of large-area devices as a function of bending cycle depending on the bending radius ( $R = 1$  and  $0.5 \text{ mm}$ ) for the  $2.5 \mu\text{m}$  thick substrate.

### Crumpling durable ultra-flexible perovskite solar cells by manipulating the neutral plane

Subsequent to the aforementioned success achieved with the 2.5-PET devices, we attempted a harsh deformation test involving crumpling and complete folding to verify the possibility of using these cells in actual wearable devices. Accordingly, we performed crumpling and folding tests as depicted in the insets in Fig. 5e and Fig. S9 (ESI<sup>†</sup>). Despite the samples being able to withstand 10 000 bending cycles with a 0.5 mm radius, they only endured fewer than 20 cycles of crumpling, even degrading immediately after folding once (Fig. S9, ESI<sup>†</sup>). As mentioned above, introduction of the parylene protective layer as a thin film on top of our full device (Fig. 5a) both modulates the NP axis onto the perovskite layer (Fig. 5b) and protects the perovskite surface from developing dead points. In order to maximize the effect of the protective layer, the NP axis where all the strains

are zero<sup>33</sup> should be located in the fragile perovskite layer.<sup>33</sup> To relocate the NP axis onto the perovskite layer, we first determined the thickness of the protective layer in accordance with eqn (1)<sup>34</sup> (see more details in Fig. S10, ESI<sup>†</sup>)

$$h = \frac{\sum_{i=1}^n E_i t_i \left[ \left( \sum_{j=1}^i t_j \right) - \frac{t_i}{2} \right]}{\sum_{i=1}^n E_i t_i} \quad (1)$$

where  $h$  denotes the distance of the neutral plane from the top surface,  $i$  is the index of each layer (parylene, copper, BCP, C<sub>60</sub>, perovskite, PEDOT:PSS, PET), and  $E_i$  and  $t_i$  are the elastic modulus and thickness of each layer  $i$ , respectively. The elastic modulus and the thicknesses of each of the layers are summarized in Table S3 (ESI<sup>†</sup>). As a result, 2.3  $\mu\text{m}$  of the protective layer is implemented for NP axis relocation onto the perovskite layer.

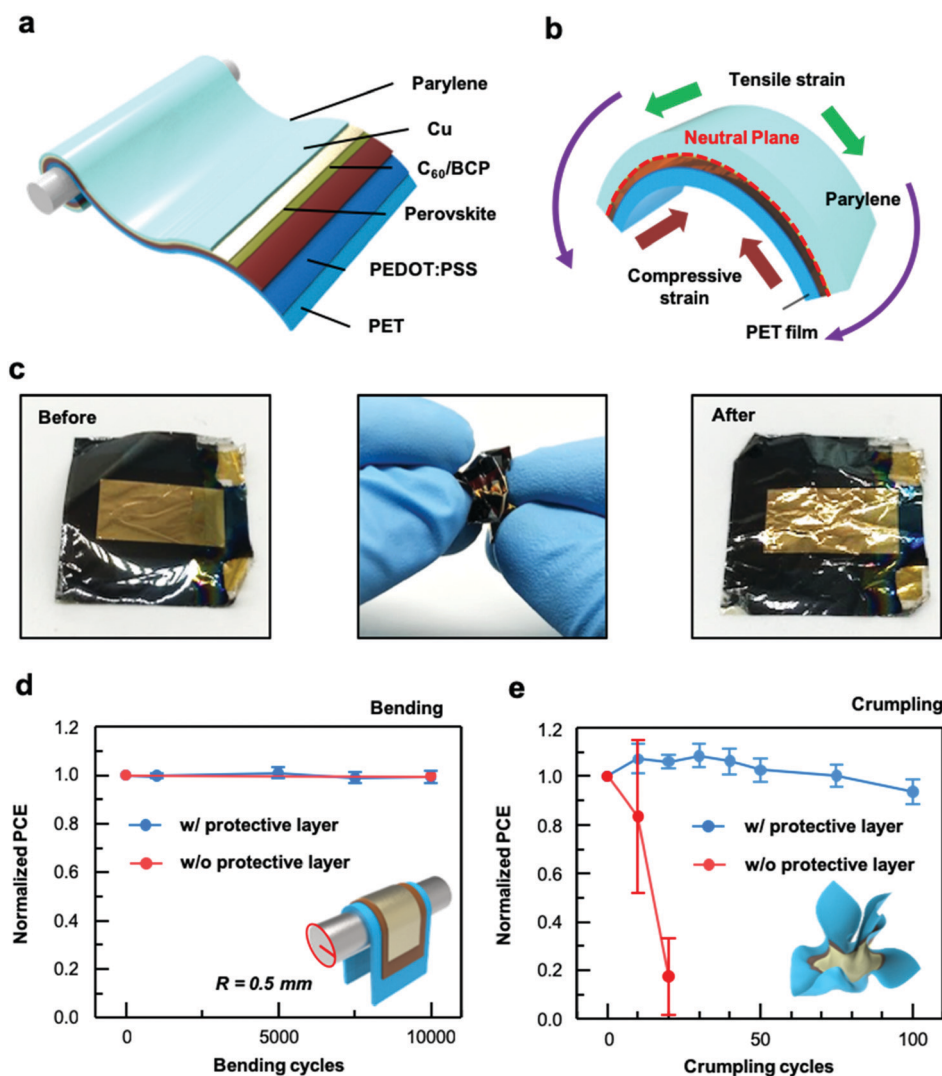


Fig. 5 Schematic illustrations of the (a) structure of the flexible perovskite solar cell with a protective layer consisting of a parylene thin film, and (b) the mechanical neutral plane located on the perovskite film, generated from the counterbalance between the compressive and tensile strain. (c) Photographic images of the devices before and after the crumpling test. Normalized power conversion efficiency (PCE) of devices as a function of (d) bending and (e) crumpling cycles with and without the protective layer (devices with an active area of  $\sim 0.09 \text{ cm}^2$ ).

Surprisingly, after applying the protective layer, the 2.5-PET devices maintain their initial performance of as much as 88% after 100 cycles of crumpling, as shown in Fig. 5e. Photographic images of the actual device with the protective layer before and after the crumpling process are presented in Fig. 5c. This is a significant result, and constitutes a breakthrough in the actual application of flexible perovskite solar cells to power wearable devices because perovskite solar cells with crumpling durability would be able to endure the wrinkling that might be produced by clothes.

## Conclusions

We investigated the mechanical properties, and specifically the development of cracks, in polycrystalline perovskite thin films by varying the substrate thickness and determining the fracture point. Knowledge of the fracture point made it possible to fabricate a crack-free perovskite thin film on an ultra-thin substrate ( $\sim 2.5 \mu\text{m}$ ). High-efficiency ultra-flexible perovskite photovoltaic devices (a PCE of 17.03%) were fabricated. These devices maintained their performance after 10 000 bending cycles at a bending radius of 0.5 mm, which is a phenomenal result. Furthermore, by employing a hybrid transparent electrode composed of a conducting polymer (PEDOT:PSS) and gold mesh grid, we successfully expanded the active area ( $1.2 \text{ cm}^2$ ), which represents an efficiency of 13.6% for an area of  $1 \text{ cm}^2$ . We additionally introduced a protective layer, which shifts the neutral plane onto the perovskite layer to further improve the mechanical durability of our device. Consequently, the flexible perovskite solar cells fabricated with the protective layer endured complete folding or crumpling for more than 100 cycles. We foresee the successful fabrication of perovskite solar cells with high mechanical durability, including the ability to endure folding and crumpling, which will contribute to the development of flexible perovskite solar cells for practical portable power sources.

## Experimental details

### Fabrication of flexible perovskite solar cells

Thin films of poly(dimethylsiloxane) (PDMS) (Dow Corning, Sylgard 184) were bonded to a glass substrate by oxygen plasma treatment (CUTE-1MPR, Femto Science Inc.). PET substrates were then attached to the PDMS/glass substrate during the fabrication process. Next, a solution of PEDOT:PSS (Clevios PH1000, Heraeus) was spin coated onto this structure at 3000 rpm for 1 min and annealed at  $120 \text{ }^\circ\text{C}$  for 20 min. This was followed by dripping methanol onto the PEDOT:PSS/PET/glass substrate during the spin-coating process at 4000 rpm for 1 min. The perovskite layer ( $\text{CH}_3\text{NH}_3\text{PbI}_3$ ), which is the light-absorbing layer, was formed on the PEDOT:PSS layer by using the Lewis base adduct method.<sup>35</sup> More specifically, a precursor solution was prepared by dissolving  $\text{PbI}_2$  (Alfa Aesar)/MAI (Xian' Chemical)/dimethyl sulfoxide (DMSO, Sigma Aldrich) in dimethyl formamide (DMF, Sigma Aldrich) in specified proportions.

This perovskite solution was spin coated at 4000 rpm for 20 s, during which diethyl ether (Sigma Aldrich) was dripped onto the coating. This was followed by annealing at  $70 \text{ }^\circ\text{C}$  for 1 min and at  $110 \text{ }^\circ\text{C}$  for 10 min. All spin-coating processes were performed inside a dry room with a relative humidity of less than 10% and a temperature of  $25 \text{ }^\circ\text{C}$ . Then, the  $\text{C}_{60}$  (20 nm)/BCP (10 nm) layer, which is the electron transport layer and the copper electrode, was deposited on the perovskite layer using a vacuum thermal evaporator. A layer of  $2.3 \mu\text{m}$  thick parylene film was coated on the flexible perovskite solar cell by using the chemical vapor deposition method as shown in Fig. S11 (ESI<sup>†</sup>).

### Preparation of the flexible substrate with a gold mesh electrode

PDMS was spin coated onto a silicon (Si) wafer at 6000 rpm for 5 min and then annealed at  $70 \text{ }^\circ\text{C}$  for 1 h. After the annealing process, a conformal method was used to attach the PET film to the PDMS/Si wafer. The gold grid electrode was designed with a width of  $2 \mu\text{m}$  and a spacing of  $200 \mu\text{m}$  and was prepared by conventional photolithography as shown in Fig. S12 (ESI<sup>†</sup>).

### FEM simulation

Two-dimensional (2D) finite element analysis of the bending experiment was conducted using ABAQUS, a commercial finite element analysis package. In this analysis, each substance layer of the solar panel is discretized by a CPS4 element (a four-node bilinear plane stress quadrilateral element). The element sizes are as follows: PET ( $0.8\text{--}1 \times 3 \mu\text{m}$ ), PEDOT:PSS ( $0.13 \times 3 \mu\text{m}$ ) and perovskite ( $0.5 \times 3 \mu\text{m}$ ). The two rigid spherical indenters and the constantly curved rigid plate were discretized by an R2D2 element (a two-node 2D linear rigid link element). The analysis was performed by changing the radius of the curved rigid plate (0.5 and 1 mm) and the thickness of the PET film (*i.e.*, 2.5, 30, and  $100 \mu\text{m}$ ). The 2D finite element analysis was performed as follows: two rigid spherical indenters, which were placed on the sides of the solar cells at a certain distance above which the perovskite, PEDOT:PSS, and PET exist, move downward to contact the upper surface of the device. After making contact, the two rigid surfaces and the solar panel move downward together to contact the upper surface of the constantly curved rigid plate. These contact and continuous downward motions induce the bending motion of the device. The downward moving motion that induces bending continues until the lower surface of the device is fully adjusted to the curvature of the curved rigid surface.

### Characterization

The  $J$ - $V$  characteristics were measured using a source meter (Keithley 2400, Tektronix) under AM 1.5G illumination at an intensity of  $100 \text{ mW cm}^{-2}$  with an Oriel S013 ATM solar simulator, which was calibrated with a KG-5 filtered standard silicon reference solar cell (91150-KG5, Newport). Our devices were measured in a glove box maintained at room temperature ( $25 \text{ }^\circ\text{C}$ ). The forward and reverse scan rates were set to 200 ms per 20 mV. EQE spectra were recorded on a Newport IQE200 system equipped with a 100 mW xenon lamp and a lock-in amplifier. The SEM images of the plane view were obtained

using a field-emission scanning electron microscope (MERLIN, Carl Zeiss), while the cross-sectional images were obtained with a focused-ion-beam (FIB) system (AURIGA, Carl Zeiss). The cyclic bending test was performed at a frequency of 1 Hz using a bending test machine (1Axis, Science Town). The crumpling durability test was performed by randomly squeezing the device as shown in Movie S1 (ESI†). The transmittance spectra of the substrates were obtained using a UV-visible spectrophotometer (Cary 5000, Agilent technologies). The sheet resistance of the transparent electrode was measured with a four-point probe (CMT-SR1000N, AIT).

## Author contributions

M. C. and H. S. J. led the study. G. L. and M.-c. K. designed experiments and analyzed the data. M. C. directed experiments and interpreted the results. G. L., M.-c. K., N. A., J. J., J. Y. performed experiments. Y. W. C., S. M. K. and D. K. contributed to the design and fabrication of substrate and electrode. J. G. L. did simulation. G. L., M.-c. K., N. A., J. G. L., H. S. J. and M. C. wrote the manuscript. All authors participated in discussion.

## Conflicts of interest

There are no conflicts to declare.

## Acknowledgements

Gunhee Lee and Min-cheol Kim contributed equally to this work. This work was supported by the Global Frontier R&D Program Center for Multiscale Energy Systems funded by the National Research Foundation under the Ministry of Science, ICT & Future Planning, Korea (2012M3A6A7054855). This work has been also supported by the National Research Foundation under the Ministry of Science and ICT, Korea (2017R1A2B3010927). We also thank T. E. Song for help with fabricating the parylene protective layer.

## Notes and references

- M. Kaltenbrunner, M. S. White, E. D. Glowacki, T. Sekitani, T. Someya, N. S. Sariciftci and S. Bauer, *Nat. Commun.*, 2012, **3**, 770.
- A. J. Baca, K. J. Yu, J. Xiao, S. Wang, J. Yoon, J. H. Ryu, D. Stevenson, R. G. Nuzzo, A. A. Rockett and Y. Huang, *Energy Environ. Sci.*, 2010, **3**, 208–211.
- B. J. Kim, D. H. Kim, Y.-Y. Lee, H.-W. Shin, G. S. Han, J. S. Hong, K. Mahmood, T. K. Ahn, Y.-C. Joo and K. S. Hong, *Energy Environ. Sci.*, 2015, **8**, 916–921.
- D. Liu and T. L. Kelly, *Nat. Photonics*, 2014, **8**, 133.
- F. Di Giacomo, A. Fakhruddin, R. Jose and T. M. Brown, *Energy Environ. Sci.*, 2016, **9**, 3007–3035.
- S. S. Shin, W. S. Yang, J. H. Noh, J. H. Suk, N. J. Jeon, J. H. Park, J. S. Kim, W. M. Seong and S. I. Seok, *Nat. Commun.*, 2015, **6**, 7410.
- C. Bi, B. Chen, H. Wei, S. DeLuca and J. Huang, *Adv. Mater.*, 2017, **29**, 1605900.
- Z. Huang, X. Hu, C. Liu, L. Tan and Y. Chen, *Adv. Funct. Mater.*, 2017, **27**, 1703061.
- D. Yang, R. Yang, X. Ren, X. Zhu, Z. Yang, C. Li and S. F. Liu, *Adv. Mater.*, 2016, **28**, 5206–5213.
- S. Song, R. Hill, K. Choi, K. Wojciechowski, S. Barlow, J. Leisen, H. J. Snaith, S. R. Marder and T. Park, *Nano Energy*, 2018, **49**, 324–332.
- H. I. Kim, M. J. Kim, K. Choi, C. Lim, Y. H. Kim, S. K. Kwon and T. Park, *Adv. Energy Mater.*, 2018, **8**, 1702872.
- X. Hu, Z. Huang, X. Zhou, P. Li, Y. Wang, Z. Huang, M. Su, W. Ren, F. Li and M. Li, *Adv. Mater.*, 2017, **29**, 1703236.
- J. Yoon, H. Sung, G. Lee, W. Cho, N. Ahn, H. S. Jung and M. Choi, *Energy Environ. Sci.*, 2017, **10**, 337–345.
- J. H. Heo, D. H. Shin, D. H. Song, D. H. Kim, S. J. Lee and S. H. Im, *J. Mater. Chem. A*, 2018, **6**, 8251–8258.
- Q. Luo, H. Ma, Q. Hou, Y. Li, J. Ren, X. Dai, Z. Yao, Y. Zhou, L. Xiang and H. Du, *Adv. Funct. Mater.*, 2018, **28**, 1706777.
- I. Jeon, T. Chiba, C. Delacou, Y. Guo, A. Kaskela, O. Reynaud, E. I. Kauppinen, S. Maruyama and Y. Matsuo, *Nano Lett.*, 2015, **15**, 6665–6671.
- Q. Luo, H. Ma, F. Hao, Q. Hou, J. Ren, L. Wu, Z. Yao, Y. Zhou, N. Wang and K. Jiang, *Adv. Funct. Mater.*, 2017, **27**, 1703068.
- Y. Jin, Y. Sun, K. Wang, Y. Chen, Z. Liang, Y. Xu and F. Xiao, *Nano Res.*, 2018, **11**, 1998–2011.
- E. Lee, J. Ahn, H. C. Kwon, S. Ma, K. Kim, S. Yun and J. Moon, *Adv. Energy Mater.*, 2018, **8**, 1702182.
- M. Kaltenbrunner, G. Adam, E. D. Glowacki, M. Drack, R. Schwödiauer, L. Leonat, D. H. Apaydin, H. Groiss, M. C. Scharber and M. S. White, *Nat. Mater.*, 2015, **14**, 1032.
- M. Park, H. J. Kim, I. Jeong, J. Lee, H. Lee, H. J. Son, D. E. Kim and M. J. Ko, *Adv. Energy Mater.*, 2015, **5**, 1501406.
- J. Feng, X. Zhu, Z. Yang, X. Zhang, J. Niu, Z. Wang, S. Zuo, S. Priya, S. Liu and D. Yang, *Adv. Mater.*, 2018, **30**, 1801418.
- K. Chu, B. G. Song, H. I. Yang, D. M. Kim, C. S. Lee, M. Park and C. M. Chung, *Adv. Funct. Mater.*, 2018, 1800110.
- K. Poorkazem, D. Liu and T. L. Kelly, *J. Mater. Chem. A*, 2015, **3**, 9241–9248.
- T. Yokota, P. Zalar, M. Kaltenbrunner, H. Jinno, N. Matsuhisa, H. Kitanosako, Y. Tachibana, W. Yukita, M. Koizumi and T. Someya, *Sci. Adv.*, 2016, **2**, e1501856.
- S. Kee, N. Kim, B. Park, B. S. Kim, S. Hong, J. H. Lee, S. Jeong, A. Kim, S. Y. Jang and K. Lee, *Adv. Mater.*, 2018, **30**, 1703437.
- S. Sun, Y. Fang, G. Kieslich, T. J. White and A. K. Cheetham, *J. Mater. Chem. A*, 2015, **3**, 18450–18455.
- Y. Rakita, S. R. Cohen, N. K. Kedem, G. Hodes and D. Cahen, *MRS Commun.*, 2015, **5**, 623–629.
- S. Kang, J. Jeong, S. Cho, Y. J. Yoon, S. Park, S. Lim, J. Y. Kim and H. J. J. o. M. C. A. Ko, *J. Mater. Chem. A*, 2019, **7**, 1107–1114.

- 30 J.-I. Park, J. H. Heo, S.-H. Park, K. I. Hong, H. G. Jeong, S. H. Im and H.-K. Kim, *J. Power Sources*, 2017, **341**, 340–347.
- 31 D. H. Kim, J. B. Whitaker, Z. Li, M. F. A. M. van Hest and K. Zhu, *Joule*, 2018, **2**, 1437–1451.
- 32 A. K. Chandiran, A. Yella, M. T. Mayer, P. Gao, M. K. Nazeeruddin and M. Grätzel, *Adv. Mater.*, 2014, **26**, 4309–4312.
- 33 S. H. Crandall, N. C. Dahl and T. J. Lardner, *An introduction to Mechanics of Solids*, McGraw-Hill Education, 1978.
- 34 D.-H. Kim, J.-H. Ahn, W. M. Choi, H.-S. Kim, T.-H. Kim, J. Song, Y. Y. Huang, Z. Liu, C. Lu and J. A. Rogers, *Science*, 2008, **320**, 507–511.
- 35 N. Ahn, D.-Y. Son, I.-H. Jang, S. M. Kang, M. Choi and N.-G. Park, *J. Am. Chem. Soc.*, 2015, **137**, 8696–8699.